ACS OMEGA

http://pubs.acs.org/journal/acsodf

Article

Boosting Hydrogen Evolution through the Interface Effects of Amorphous $NiMoO_4$–MoO_2 and Crystalline Cu

Yue Yao,[†] Enlai Hu,[†] Zhiyu Wang, Yuanjing Cui, and Guodong Qian*

Cite This: *ACS Omega* 2022, 7, 2244–2251

Read Online

ACCESS | Metrics & More | Article Recommendations | Supporting Information

ABSTRACT: The rational design and synthesis of a highly efficient and cost-effective electrocatalyst for hydrogen evolution reaction (HER) are of great importance for the efficient generation of sustainable energy. Herein, amorphous/crystalline heterophase Ni–Mo–O/Cu (denoted as a/c Ni–Mo–O/Cu) was synthesized by a one-pot electrodeposition method. Thanks to the introduction of metallic Cu and the formation of amorphous Ni–Mo–O, the prepared electrocatalyst exhibits favorable conductivity and abundant active sites, which are favorable to the HER progress. Moreover, the interfaces consisting of Cu and Ni–Mo–O show electron transfers between these components, which might modify the absorption/desorption energy of H atoms, thus accelerating HER activity. As expected, the prepared a/c Ni–Mo–O/Cu possesses excellent HER performance, which affords an ultralow overpotential of 34.8 mV at 10 mA cm^{-2}, comparable to that of 20 wt % Pt/C (35.0 mV), and remarkable stability under alkaline conditions.

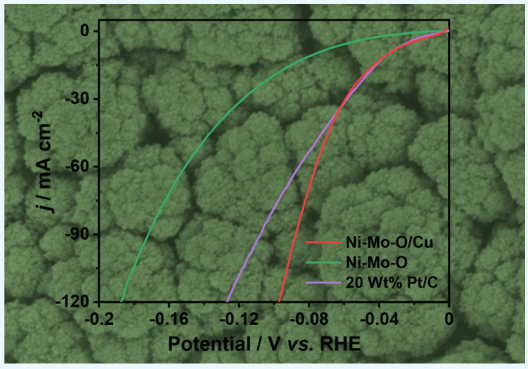

1. INTRODUCTION

Rapid consumption of chemical fossil fuels aggravates the energy crisis and environmental pollution, thus highly demanding for renewable and clean energy.[1] With the merits of high energy density and environmental friendliness, hydrogen is an ideal energy carrier to address the energy crisis.[2−4] Among the various hydrogen generation approaches, water electrolysis might be the most promising, clean, and attractive way for the future hydrogen cycle.[5,6] To lower the overpotential of hydrogen evolution reaction (HER), especially in alkaline media, electrocatalysts with high activity are urgently required. Although Pt-based materials exhibit prominent HER activity under alkaline conditions, scarcity, high cost, and instability of these electrocatalysts severely impede their wide applications.[7−9] Therefore, it is highly urgent to develop active, stable, and noble metal-free alternatives for an efficient HER under alkaline conditions.[10−12] Among various alternatives, Ni/Mo-based oxides have been widely reported as HER electrocatalysts because of their favorable stability and facilely regulable electronic structure.[13−17] Nevertheless, the intrinsically poor conductivity of these oxides hinders their overall efficiency, which requires efficient strategies to improve this situation.

To date, various approaches have been proposed for the design of superior electrocatalysts, such as composition regulation,[18−26] size/morphology construction,[27] and crystallinity modification.[28−30] In this regard, heterostructure development to form interfaces is a promising and intriguing method, which can accelerate the electron transfer rate, redistribute the electron density, and regulate the absorption/desorption energy of intermediates.[22,23] Furthermore, more active sites can be exposed after forming interfaces, which is another reason for the enhanced electrochemical activity.[31] In addition, developing amorphous electrocatalysts is also an attractive method to increase active site density. Benefitting from short-range structural ordering, amorphous materials always possess abundant unsaturated bands that can be electrochemical reaction sites.[29,32,33] Therefore, it is meaningful to design and synthesize amorphous/crystalline heterophase nanomaterials that will not only regulate the electronic structure but also maximize the active site density.[34−36] However, the poor conductivity of amorphous materials needs to be improved, which is one of the crucial key points for the excellent electrochemical activity. Moreover, it is a challenge to synthesize amorphous Ni–Mo oxides, due to the lack of an efficiently synthetic approach.

Encouraged by the aforementioned concerns, amorphous/crystalline heterophase Ni–Mo–O/Cu (denoted as a/c Ni–Mo–O/Cu) was fabricated as a highly efficient HER electrocatalyst by a facile one-step electrodeposition method. Electrochemical tests reveal that metallic Cu in this hybrid is key for the enhanced conductivity and redistribution of

Received: October 18, 2021
Accepted: December 22, 2021
Published: January 3, 2022

https://doi.org/10.1021/acsomega.1c05844
ACS Omega 2022, 7, 2244–2251

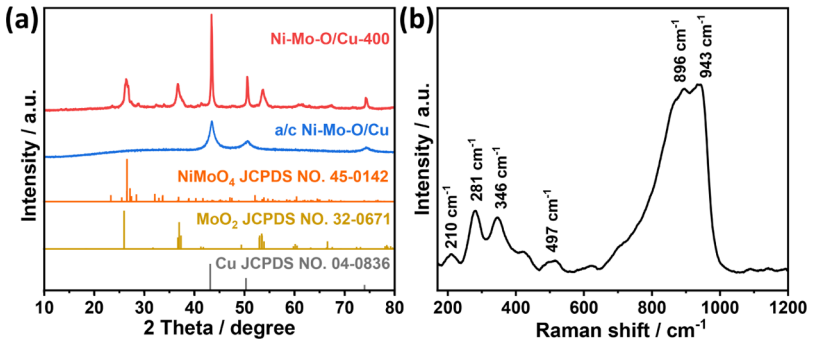

Figure 1. (a) XRD patterns of a/c Ni−Mo−O/Cu and Ni−Mo−O/Cu-400. (b) Raman spectra of a/c Ni−Mo−O/Cu.

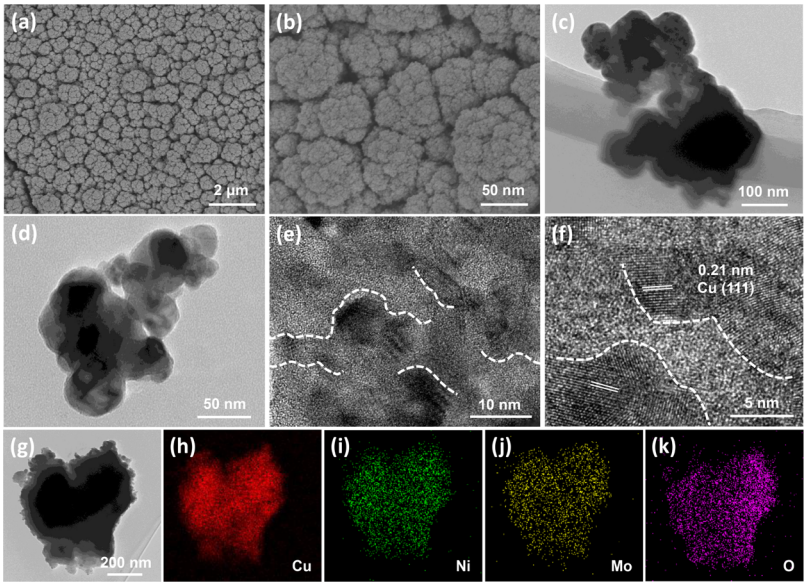

Figure 2. (a,b) FESEM image, (c,d) TEM image, and (e,f) HRTEM image of a/c Ni−Mo−O/Cu. (g) TEM image and the corresponding EDS mapping images of (h) Cu, (i) Ni, (j) Mo, and (k) O in a/c Ni−Mo−O/Cu.

electron density, while Ni−Mo−O provides abundant active centers for the HER. Featured with favorable conductivity, abundant interfaces, and efficient electron transfer rate, the prepared a/c Ni−Mo−O/Cu electrocatalyst exhibits an ultralow overpotential (34.8 mV at 10 mV cm^{-2}) and Tafel slope (38.7 mV dec^{-1}) and also remarkable stability that are comparable or even superior to those of the 20 wt % Pt/C benchmark.

2. RESULTS AND DISCUSSION

2.1. Characterizations. The crystalline phase of the as-prepared samples was characterized by X-ray diffraction (XRD). As shown in Figure 1a, only a broad peak at about 30° and three strong peaks indexed to metallic Cu (JCPDS no. 04-0836) were detected for a/c Ni−Mo−O/Cu (scratched from the substrate), suggesting the existence of amorphous components. To further identify the component of the amorphous phase, annealing treatment was conducted to improve the crystallinity of a/c Ni−Mo−O/Cu. After annealing at 400 °C in a N_2 atmosphere for 2 h, the XRD pattern (Figure 1a) reveals the formation of $NiMoO_4$ (JCPDS no. 45-0142) and MoO_2 (JCPDS no. 32-0671), implying that the as-prepared a/c Ni−Mo−O/Cu electrocatalyst consists of amorphous Ni−Mo−O and crystalline Cu. The Raman spectrum was further collected to verify the existence of $NiMoO_4$ and MoO_2 (Figure 1b). Raman peaks at 210, 281, and 497 cm^{-1} can be associated to the characteristic of MoO_2.[37,38] The other peaks at 346, 896, and 943 cm^{-1} correspond to the Mo−O bending modes and symmetric and asymmetric stretching modes of $NiMoO_4$, consistent with the previous studies.[39,40] For comparison, Ni−Mo−O and Cu electrodes were also fabricated. XRD patterns (Figure S1) demonstrated that the Ni−Mo−O electrode consists of amorphous $NiMoO_4$ and MoO_2, and the Cu electrode only contains a single component of metallic Cu. The formation mechanism was proposed as follows, according to the previous studies.[41,42] First, metallic Ni and Cu could be precipitated with the assistance of NH_4^+ under such a large cathodic current. Simultaneously, the transformation from MoO_4^{2-} to amorphous MoO_2 occurred under the reduction potential. It is worth noting that during the electrodeposition process, a water splitting reaction took place as well and O_2 bubbles were released from the anode. Then, the obtained Ni and partial MoO_2 were oxidized to amorphous $NiMoO_4$ with the assistance of O_2 filled in the electrolyte. Finally, the ternary composite consisting of amorphous Ni−Mo−O and crystalline Cu was successfully synthesized by a facile one-step electrodeposition method for 250 s. The reaction equations can be expressed as follows

https://doi.org/10.1021/acsomega.1c05844
ACS Omega 2022, 7, 2244−2251

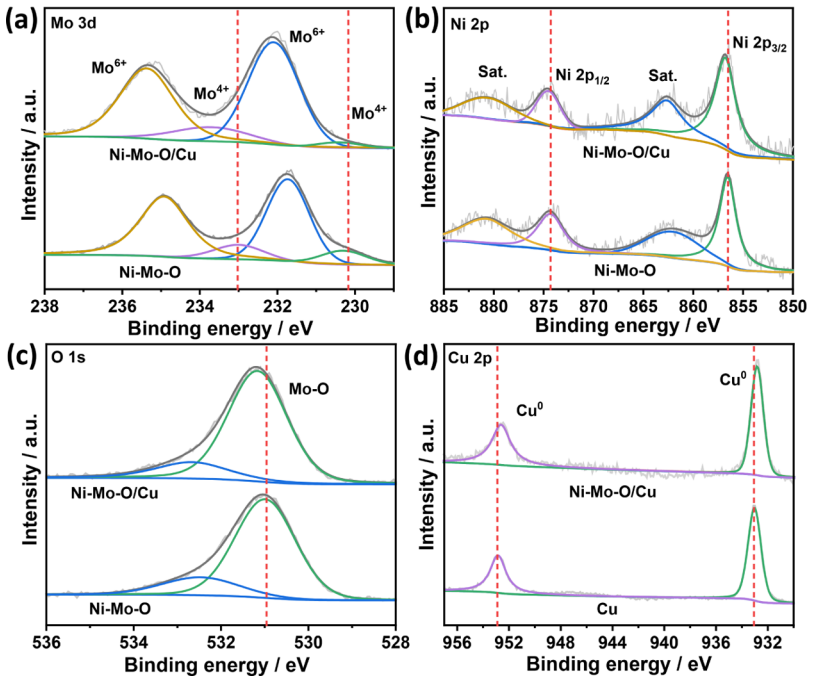

Figure 3. High-resolution (a) Mo 3d spectrum, (b) Ni 2p spectrum, and (c) O 1s spectrum of a/c Ni−Mo−O/Cu and Ni−Mo−O. (d) High-resolution Cu 2p spectrum of a/c Ni−Mo−O/Cu and Cu.

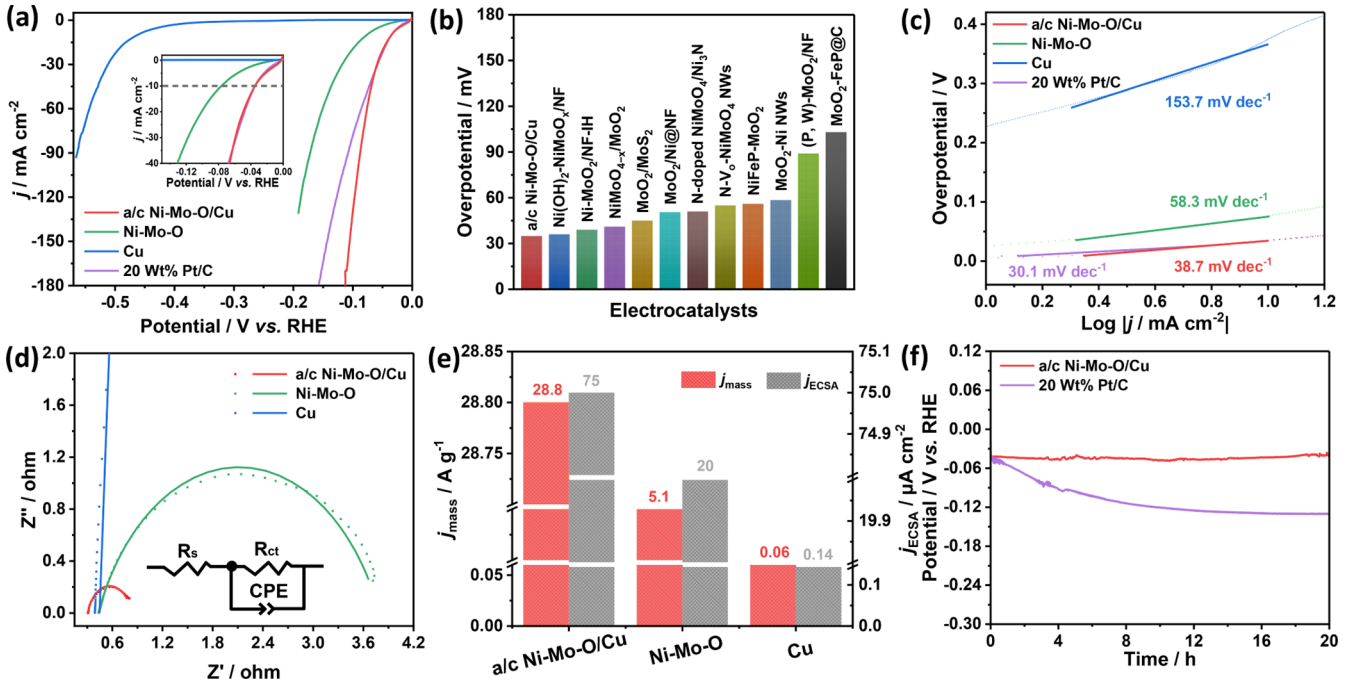

Figure 4. (a) Polarization curves of a/c Ni−Mo−O/Cu, Ni−Mo−O, Cu, and 20 wt % Pt/C. (b) Overpotentials at 10 mA cm^{-2} for a/c Ni−Mo−O/Cu and other recently reported electrocatalysts. (c) Tafel slopes of a/c Ni−Mo−O/Cu, Ni−Mo−O, Cu, and 20 wt % Pt/C. (d) Nyquist plots and the corresponding fitting results of a/c Ni−Mo−O/Cu, Ni−Mo−O, and Cu. (e) Mass activity and ECSA-normalized activity for a/c Ni−Mo−O/Cu, Ni−Mo−O, and Cu at an overpotential of 100 mV. (f) Chronopotentiometry curves of a/c Ni−Mo−O/Cu and 20 wt % Pt/C at 10 mA cm^{-2}.

$$Ni^{2+} + 2NH_4^+ + 4e^- \rightarrow Ni + 2NH_3 + H_2 \quad (1)$$

$$MoO_4^{2-} + 4H^+ + 2e^- \rightarrow MoO_2 + 2H_2O \quad (2)$$

$$Ni + MoO_2 + O_2 \rightarrow NiMoO_4 \quad (3)$$

$$Cu^{2+} + 2NH_4^+ + 4e^- \rightarrow Cu + 2NH_3 + H_2 \quad (4)$$

To elucidate the morphology and microstructure of the obtained electrocatalysts, field-emission scanning electron microscopy (FESEM) and transmission electron microscopy (TEM) measurements were performed. As shown in the FESEM image (Figure 2a,b), a/c Ni−Mo−O/Cu is composed of numerous nanoparticles with the shape of a cauliflower. The TEM image (Figure 2c,d) also confirms the assembled

https://doi.org/10.1021/acsomega.1c05844
ACS Omega 2022, 7, 2244−2251

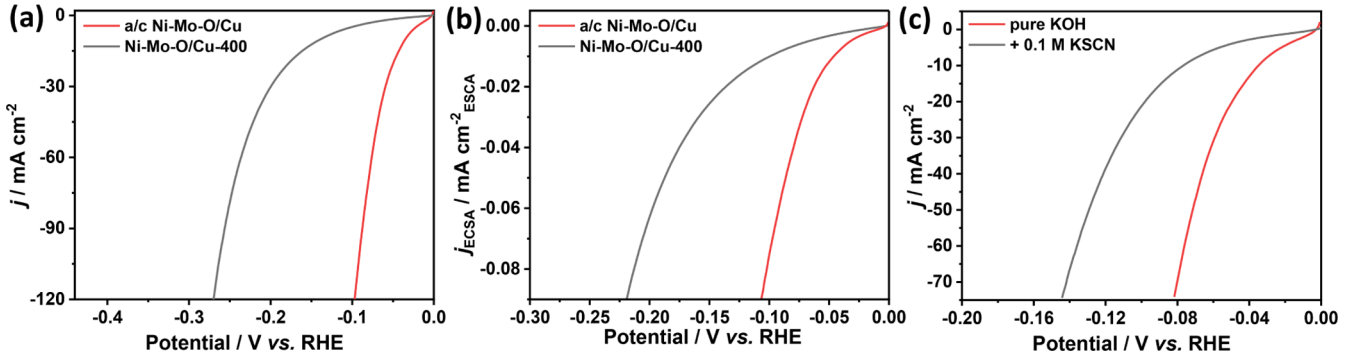

Figure 5. (a) Polarization curves and (b) ECSA-normalized polarization curves of a/c Ni−Mo−O/Cu and Ni−Mo−O/Cu-400. (c) Poison measurements with SCN^- of a/c Ni−Mo−O/Cu.

nanoparticles with a size ranging from 20 to 50 nm. The high-resolution TEM (HRTEM) image (Figure 2e,f) of a/c Ni−Mo−O/Cu clearly reveals the amorphous and crystalline components. In the crystalline component, the lattice fringe of 0.21 nm can be indexed to the (111) planes of metallic Cu. For the amorphous part, the absence of crystal fringes indicates the existence of amorphous Ni−Mo−O, which is consistent with the XRD results. It is worth noting that the ternary composite with abundant amorphous/crystalline interfaces could regulate electronic structures, provide considerable active sites, and improve electron transfer rate. Moreover, energy-dispersive X-ray spectroscopy (EDS) mapping images (Figure 2g−k) elucidate the homogeneous distribution of Ni, Mo, Cu, and O in a/c Ni−Mo−O/Cu. Inductively coupled plasma (ICP) tests reveal that the mass ratio of Ni, Mo, and Cu elements in Ni−Mo−O/Cu is about 45:17:38 (Table S1).

Generally, surface properties of electrocatalysts could have great influence on their electrochemical performance. It is necessary to reveal the surface chemical compositions and the electronic states of the as-prepared electrocatalysts by X-ray photoelectron spectroscopy (XPS) tests. As shown in Figure S4a, the survey XPS spectrum of a/c Ni−Mo−O/Cu verifies the existence of Ni, Mo, Cu, and O. For the high-resolution Mo 3d spectrum (Figure 3a), peaks at 230.42 and 233.72 eV are characteristic for Mo^{4+} species, indicating the presence of MoO_2, and the peaks at 232.09 and 235.37 eV are in agreement with Mo^{6+} species for $NiMoO_4$.[43,44] The fitted Ni 2p spectrum (Figure 3b) displays spin−orbit doublets at 856.78 and 874.52 eV and two satellite peaks at 862.61 and 880.62 eV, which reveal the Ni^{2+} species in $NiMoO_4$.[45,46] In the O 1s spectrum (Figure 3c), two peaks at 531.16 and 532.67 eV can be assigned to the Mo−O bonding mode and the hydroxyl species of adsorbed H_2O, respectively.[41,47] The metallic Cu in the composite was further confirmed by the Cu 2p spectrum (Figure 3d), in which two peaks at 932.82 and 952.61 eV assigned to Cu^0 species are detected.[48,49] Interestingly, the typical peaks of Ni, Mo, and O for a/c Ni−Mo−O/Cu have a positive shift compared with those of Ni−Mo−O, whereas the binding energies of Cu for a/c Ni−Mo−O/Cu are lower than those of the Cu electrocatalyst. The abovementioned results suggest the existence of strong electron interactions between amorphous Ni−Mo−O and metallic Cu components, implying the redistribution of electron density at the interface. According to the previous studies, the electron transfers from Ni−Mo−O to Cu might optimize the adsorption/desorption energy of the intermediates to maximize the electrochemical activity of the electrocatalysts.[50]

2.2. HER Performance. The HER performance of a/c Ni−Mo−O/Cu was investigated in a traditional three-electrode cell with 1.0 M KOH as the electrolyte. With the *iR*-compensated polarization curves presented in Figure 4a, the overpotential of a/c Ni−Mo−O/Cu is merely 34.8 mV at 10 mA cm^{-2}, which is much lower than that of Ni−Mo−O (76.3 mV) and Cu (462.1 mV) electrodes. Such outstanding HER activity is also comparable to that of 20 wt % Pt/C (35.0 mV) and even superior to that of most of the non-noble metal-based electrocatalysts reported in recent years (Figure 4b and Table S2). Tafel slopes obtained from polarization curves are shown in Figure 4c. The a/c Ni−Mo−O/Cu electrode has the smallest Tafel slope of 38.7 mV dec^{-1} compared to that of Ni−Mo−O (58.3 mV dec^{-1}) and Cu (153.7 mV dec^{-1}), implying that the a/c Ni−Mo−O/Cu electrode exhibits favorable kinetics. Electrochemical impedance spectroscopy (EIS) results were recorded to further study the charge-transfer kinetics of the as-prepared electrocatalysts. Nyquist plots and the corresponding fitting results (Figure 4d) show that the a/c Ni−Mo−O/Cu electrode has the smallest charge transfer resistance (R_{ct}) among all of the contrast samples, which suggests its favorable electrochemical kinetics and electron transfer rate.[51]

Mass activity (normalized to the mass loading of the electrocatalyst), one of the crucial evaluation factors for the practical application of electrocatalysts, is also calculated to further assess the electrocatalytic activity for the obtained electrode.[52,53] As seen in the mass-normalized polarization curves (Figure S6a), the mass activity for a/c Ni−Mo−O/Cu at the overpotential of 100 mV is 28.8 A g^{-1}, which is about 5.6 and 480 times larger than that of Ni−Mo−O (5.1 A g^{-1}) and Cu (0.06 A g^{-1}) electrodes, respectively (Figure 4e). The high mass activity of a/c Ni−Mo−O/Cu implies its outstanding intrinsic HER activity. To further exclude the influence of the electrochemical active surface area (ECSA) on the HER activity, the ECSA-normalized polarization curves were also collected. According to the cyclic voltammetry (CV) results, a/c Ni−Mo−O/Cu exhibits the highest ECSA with a value of 1726 (Figure S7), which might be one of the reasons for its remarkable HER activity. After normalized to ECSA, a/c Ni−Mo−O/Cu still outputs the largest current at the same overpotential (Figures 4e and S6b), which further provides solid evidence to verify its high intrinsic HER activity. Long-term durability, another crucial evaluation factor, was also tested. Figure 4f illustrates that the potential for a/c Ni−Mo−

https://doi.org/10.1021/acsomega.1c05844
ACS Omega 2022, 7, 2244−2251

O/Cu at a current density of 10 mA cm^{-2} can be well preserved for 20 h, while it has a quick increase for the 20 wt % Pt/C benchmark, which implies the good stability of a/c Ni−Mo−O/Cu as a non-noble metal-based electrocatalyst for the HER. Furthermore, FESEM, TEM, and XPS (Figures S8−S10) results of the post-HER a/c Ni−Mo−O/Cu are consistent with those of pristine ones, demonstrating the excellent stability of a/c Ni−Mo−O/Cu. The outstanding activity and durability make a/c Ni−Mo−O/Cu a promising HER electrocatalyst.

2.3. Discussion. The prominent HER performance of a/c Ni−Mo−O/Cu can be attributed to its amorphous feature, abundant interfaces, and specific active materials. On one hand, the amorphous feature endows the a/c Ni−Mo−O/Cu electrode with a higher active site density than the crystalline counterpart because of their abundant randomly oriented bonds.[28−30] CV results reveal that the ECSA decreases to 480 cm^2 after annealing at 400 °C (Figure S11). Correspondingly, the overpotential of Ni−Mo−O/Cu-400 at 10 mA cm^{-2} increased to 138.5 mV (Figure 5a). On the other hand, the structural flexibility characteristic of amorphous materials allows the electrocatalysts to self-regulate themselves for the optimal volume and surface to have enhanced electrochemical activity.[29] As demonstrated by ECSA-normalized polarization curves (Figure 5b), a dramatic decline in current output can be observed for Ni−Mo−O/Cu-400. Generally, amorphous materials have poor conductivity that is unfavorable to the electrochemical performance. Fortunately, the seamless connection between Ni−Mo−O and Cu guarantees high electron transfer rate (Figure 4d) for the electrocatalyst. Moreover, the interface renders the redistribution of electron density between Ni−Mo−O and Cu, which could optimize the adsorption/desorption energy of hydrogen atoms.[50]

To illustrate the crucial importance of the Ni−Mo−O component, SCN^- poison measurements were conducted based on the poison effect of SCN^- ions for oxidized metal species during the electrocatalytic process.[54,55] As shown in Figure S12, the ECSA for a/c Ni−Mo−O/Cu and Ni−Mo−O obviously decreased after introducing 0.1 M SCN^- into the electrolyte, whereas it almost has no change for the Cu electrode under the same conditions. The aforementioned results suggest that SCN^- indeed only poisons the oxidized metal species (Ni^{2+} and $Mo^{4/6+}$), while having negligible influence on metallic sites (Cu^0). Polarization curves (Figures 5c and S13a) reveal that the HER activities of a/c Ni−Mo−O/Cu and Ni−Mo−O significantly decrease in 1.0 M KOH with 0.1 M KSCN, which implies that $NiMoO_4$ and MoO_2 are the major active materials. In contrast, the polarization curve of the poisoned measurement for Cu is similar with that of the pristine one (Figure S13b). Based on the aforementioned results, it can be deduced that Ni−Mo−O is the main active center for the HER, and Cu plays a vital role in the redistribution of electron density and the promotion of electron transfer rate.[54,56]

3. CONCLUSIONS

In summary, we have established a noble metal-free electrocatalyst, a/c Ni−Mo−O/Cu, for a highly efficient HER under alkaline conditions, which can be facilely synthesized by a one-pot electrodeposition strategy. Benefitting from the advantages of the amorphous nature, numerous interfaces, and specific active materials, the as-prepared a/c Ni−Mo−O/Cu has abundant active sites, a fast electron transfer rate, and a robust structure. As expected, a/c Ni−Mo−O/Cu exhibits excellent HER activity with an ultralow overpotential (34.8 mV at 10 mA cm^{-2}) and a small Tafel slope (38.7 mV dec^{-1}) that are comparable to those of the 20 wt % Pt/C benchmark (35.0 mV at 10 mA cm^{-2}, 30.1 mV dec^{-1}). Moreover, a/c Ni−Mo−O/Cu also displays prominent stability, which can homogeneously catalyze hydrogen evolution for 20 h. The outstanding HER activity and stability indicate that the prepared a/c Ni−Mo−O/Cu is a promising HER electrocatalyst under alkaline conditions.

4. EXPERIMENTAL SECTION

4.1. Materials. Nickel(II) chloride hexahydrate ($NiCl_2·6H_2O$) and potassium thiocyanate (KSCN) are purchased from Shanghai Aladdin Biochemical Technology Co., Ltd. Ammonium molybdate(VI) tetrahydrate [$(NH_4)_6Mo_7O_{24}·4H_2O$], copper(II) chloride dihydrate ($CuCl_2·2H_2O$), ammonium chloride (NH_4Cl), and potassium hydroxide (KOH) were purchased from Sinopharm Chemical Reagent Co., Ltd. Commercial Pt/C (20 wt %) was purchased from SCI Materials Hub.

4.2. Synthesis of a/c Ni−Mo−O/Cu, Ni−Mo−O, and Cu Electrodes. The a/c Ni−Mo−O/Cu was synthesized through a one-step electrodeposition method with a conventional two-electrode system at room temperature. Typically, 1.66 g of $NiCl_2·6H_2O$, 0.21 g of $(NH_4)_6Mo_7O_{24}·4H_2O$, 0.10 g of $CuCl_2·2H_2O$, and 3.75 g of NH_4Cl were dissolved into 70 mL of deionized water to obtain the electrodeposition electrolyte. The electrodeposition was performed at a constant current of −250 mA for 250 s using a piece of Cu foam (1 × 1 cm^2) as a working electrode and a carbon electrode as a counter electrode. The prepared electrode was washed with deionized water three times for further use. In addition, contrast experiments were carried out to determine the optimum conditions for the fabrication of a/c Ni−Mo−O/Cu, such as different contents of components and different deposition times. Typically, the Ni−Mo−O electrode was synthesized by a similar process without adding $CuCl_2·2H_2O$ into the electrodeposition electrolyte. For the Cu electrode, the electrolyte was prepared by dissolving 0.10 g of $CuCl_2·2H_2O$ and 3.75 g of NH_4Cl into 70 mL of deionized water, while other conditions were unchanged. Moreover, the crystalline Ni−Mo−O/Cu and Ni−Mo−O electrodes were obtained by heating a/c Ni−Mo−O/Cu and Ni−Mo−O for 2 h at 400 °C under N_2 flow with a rate of 5 °C min^{-1} (named as Ni−Mo−O/Cu-400 and Ni−Mo−O-400, respectively).

4.3. Characterizations. XRD patterns were collected using a Shimadzu XRD7000 powder XRD instrument with Cu K_α radiation (λ = 1.5416 Å). Before the XRD tests, the active materials were scratched from the Cu foam to avoid the influence of the strong XRD peaks from the Cu foam. A Hitachi S-4800 field emission scanning electron microscope and FEI Tecnai G^2 F20 S-TWIN transmission electron microscope were used to elucidate the morphology of electrocatalysts. Raman spectra were examined on a HORIBA Scientific LabRAM HR evolution spectrometer with an excitation laser beam wavelength of 514 nm. ICP spectroscopy was tested using a Thermo IRIS Intrepid II XSP spectrometer. XPS measurements were carried out on a Thermo Scientific K-Alpha X-ray photoelectron spectrometer with the correction of binding energy by C 1s at 284.6 eV.

4.4. Electrochemical Measurements. The electrochemical tests were performed on a 660E CH Instruments

https://doi.org/10.1021/acsomega.1c05844
ACS Omega 2022, 7, 2244−2251

electrochemical workstation in 1.0 M KOH aqueous solution (pH = 13.8) at room temperature. A three-electrode system was adopted with a saturated calomel electrode (SCE, saturated KCl) as a reference electrode, a carbon rod as counter electrode, and the obtained electrode as a working electrode. For the fabrication of the Pt/C electrode as a benchmark, 5 mg of commercial Pt/C (20 wt %) was dispersed into a mixed solution with 490 μL of ethanol and 10 μL of Nafion solution (5 wt %) with sonication. After 60 min, 100 μL of homogeneous ink was dropped onto a Cu foam with a size of 1 × 1 cm^2. All potentials were converted to the reversible hydrogen electrode (RHE) scale: $E_{(RHE)} = E_{(SCE)} + 0.241 + 0.059pH$. The polarization curves were recorded at a scan rate of 2 mV s^{-1}, and *iR* compensation was applied for all of them. EIS was collected under a constant overpotential of 100 mV with frequency ranging from 10^5 to 0.01 Hz and 5 mV sinusoidal perturbations. CV measurements were performed in a potential range of 0.1−0.2 V versus RHE at scan rates of 2, 4, 6, 8, and 10 mV s^{-1}. Double-layer capacitance (C_{dl}) was calculated by plotting $|j_a - j_c|$ against scan rates, and the half of the slope was the value of C_{dl}. The ECSA was further determined by C_{dl}. Chronopotentiometry tests were carried out under a constant current density of 10 mA cm^{-2} to evaluate the long-term durability of the electrocatalysts.

■ ASSOCIATED CONTENT

Supporting Information

The Supporting Information is available free of charge at https://pubs.acs.org/doi/10.1021/acsomega.1c05844.

XRD patterns of Ni−Mo−O, Ni−Mo−O-400, and Cu; FESEM images and XPS survey spectra of a/c Ni−Mo−O/Cu, Ni−Mo−O, and Cu; EDS and polarization curves of a/c Ni−Mo−O/Cu with different reaction conditions; mass-normalized and ECSA-normalized polarization curves, CV curves, and linear plots of capacitive currents as a function of scan rates for a/c Ni−Mo−O/Cu, Ni−Mo−O, and Cu; FESEM images, TEM image, HRTEM image, and XPS spectra of a/c Ni−Mo−O/Cu after stability test; CV curves and linear plots of capacitive currents as a function of scan rates for Ni−Mo−O/Cu-400 and a/c Ni−Mo−O/Cu, Ni−Mo−O, and Cu in a mixed electrolyte with 1.0 M KOH and 0.1 M KSCN; poison measurements with SCN^- of Ni−Mo−O and Cu; HER performance comparison; and mass loading of a/c Ni−Mo−O/Cu, Ni−Mo−O, and Cu (PDF)

■ AUTHOR INFORMATION

Corresponding Author

Guodong Qian − *State Key Laboratory of Silicon Materials, Cyrus Tang Center for Sensor Materials and Applications, School of Materials Science and Engineering, Zhejiang University, Hangzhou 310027, China;* orcid.org/0000-0001-7133-2473; Email: gdqian@zju.edu.cn

Authors

Yue Yao − *State Key Laboratory of Silicon Materials, Cyrus Tang Center for Sensor Materials and Applications, School of Materials Science and Engineering, Zhejiang University, Hangzhou 310027, China*

Enlai Hu − *State Key Laboratory of Silicon Materials, Cyrus Tang Center for Sensor Materials and Applications, School of Materials Science and Engineering, Zhejiang University, Hangzhou 310027, China*

Zhiyu Wang − *State Key Laboratory of Silicon Materials, Cyrus Tang Center for Sensor Materials and Applications, School of Materials Science and Engineering, Zhejiang University, Hangzhou 310027, China;* orcid.org/0000-0002-4908-8264

Yuanjing Cui − *State Key Laboratory of Silicon Materials, Cyrus Tang Center for Sensor Materials and Applications, School of Materials Science and Engineering, Zhejiang University, Hangzhou 310027, China;* orcid.org/0000-0002-9084-878X

Complete contact information is available at: https://pubs.acs.org/10.1021/acsomega.1c05844

Author Contributions

†Y.Y. and E.H. contributed equally to this work.

Notes

The authors declare no competing financial interest.

■ ACKNOWLEDGMENTS

This work was supported by the National Natural Science Foundation of China (51632008 and 61721005).

■ REFERENCES

(1) Christopher, P.; Xin, H.; Linic, S. Visible-Light-Enhanced Catalytic Oxidation Reactions on Plasmonic Silver Nanostructures. *Nat. Chem.* **2011**, *3*, 467−472.

(2) Dunn, S. Hydrogen Futures: Toward a Sustainable Energy System. *Int. J. Hydrogen Energy* **2002**, *27*, 235−264.

(3) Yu, Z.-Y.; Lang, C.-C.; Gao, M.-R.; Chen, Y.; Fu, Q.-Q.; Duan, Y.; Yu, S.-H. Ni-Mo-O Nanorod-Derived Composite Catalysts for Efficient Alkaline Water-to-Hydrogen Conversion via Urea Electrolysis. *Energy Environ. Sci.* **2018**, *11*, 1890−1897.

(4) Wu, T.; Dong, C.; Sun, D.; Huang, F. Enhancing Electrocatalytic Water Splitting by Surface Defect Engineering in Two-Dimensional Electrocatalysts. *Nanoscale* **2021**, *13*, 1581−1595.

(5) Yusuf, B. A.; Xie, M.; Yaseen, W.; Xie, J.; Xu, Y. Hierarchical Ultrathin Defect-Rich $CoFe_2O_4$@BC Nanoflowers Synthesized via a Temperature-Regulated Strategy with Outstanding Hydrogen Evolution Reaction Activity. *Inorg. Chem. Front.* **2021**, *8*, 1455−1467.

(6) Sun, L.; Luo, Q.; Dai, Z.; Ma, F. Material Libraries for Electrocatalytic Overall Water Splitting. *Coord. Chem. Rev.* **2021**, *444*, 214049.

(7) Hu, E.; Yao, Y.; Cui, Y.; Qian, G. Strategies for the Enhanced Water Splitting Activity over Metal-Organic Frameworks-Based Electrocatalysts and Photocatalysts. *Mater. Today Nano* **2021**, *15*, 100124.

(8) Hu, E.; Feng, Y.; Nai, J.; Zhao, D.; Hu, Y.; Lou, X. W. Construction of Hierarchical Ni-Co-P Hollow Nanobricks with Oriented Nanosheets for Efficient Overall Water Splitting. *Energy Environ. Sci.* **2018**, *11*, 872−880.

(9) Cheng, W.; Zhang, H.; Luan, D.; Lou, X. W. Exposing Unsaturated Cu_1-O_2 Sites in Nanoscale Cu-MOF for Efficient Electrocatalytic Hydrogen Evolution. *Sci. Adv.* **2021**, *7*, No. eabg2580.

(10) Zhang, H.; Cheng, W.; Luan, D.; Lou, X. W. Atomically Dispersed Reactive Centers for Electrocatalytic CO_2 Reduction and Water Splitting. *Angew. Chem., Int. Ed.* **2021**, *60*, 13177−13196.

(11) Jin, H.; Wang, X.; Tang, C.; Vasileff, A.; Li, L.; Slattery, A.; Qiao, S. Z. Stable and Highly Efficient Hydrogen Evolution From Seawater Enabled by an Unsaturated Nickel Surface Nitride. *Adv. Mater.* **2021**, *33*, 2007508.

(12) Wang, X.; Zheng, Y.; Sheng, W.; Xu, Z. J.; Jaroniec, M.; Qiao, S.-Z. Strategies for Design of Electrocatalysts for Hydrogen Evolution under Alkaline Conditions. *Mater. Today* **2020**, *36*, 125−138.

(13) Zhang, Z.; Ma, X.; Tang, J. Porous $NiMoO_{4-x}/MoO_2$ Hybrids as Highly Effective Electrocatalysts for the Water Splitting Reaction. *J. Mater. Chem. A* **2018**, *6*, 12361−12369.
(14) Fei, B.; Chen, C.; Hu, C.; Cai, D.; Wang, Q.; Zhan, H. Engineering One-Dimensional Bunched Ni-MoO_2@Co-CoO-NC Composite for Enhanced Lithium and Sodium Storage Performance. *ACS Appl. Energy Mater.* **2020**, *3*, 9018−9027.
(15) Liang, W.; Dong, P.; Le, Z.; Lin, X.; Gong, X.; Xie, F.; Zhang, H.; Chen, J.; Wang, N.; Jin, Y.; Meng, H. Electron Density Modulation of MoO_2/Ni to Produce Superior Hydrogen Evolution and Oxidation Activities. *ACS Appl. Mater. Interfaces* **2021**, *13*, 39470−39479.
(16) Xiong, G.; Chen, Y.; Zhou, Z.; Liu, F.; Liu, X.; Yang, L.; Liu, Q.; Sang, Y.; Liu, H.; Zhang, X.; Jia, J.; Zhou, W. Rapid Synthesis of Various Electrocatalysts on Ni Foam Using a Universal and Facile Induction Heating Method for Efficient Water Splitting. *Adv. Funct. Mater.* **2021**, *31*, 2009580.
(17) Wang, C.; Tian, Y.; Gu, Y.; Xue, K.-H.; Sun, H.; Miao, X.; Dai, L. Plasma-Induced Moieties Impart Super-Efficient Activity to Hydrogen Evolution Electrocatalysts. *Nano Energy* **2021**, *85*, 106030.
(18) Li, L.; Li, G.; Zhang, Y.; Ouyang, W.; Zhang, H.; Dong, F.; Gao, X.; Lin, Z. Fabricating Nano-IrO_2@Amorphous Ir-MOF Composites for Efficient Overall Water Splitting: a One-Pot Solvothermal Approach. *J. Mater. Chem. A* **2020**, *8*, 25687−25695.
(19) Yan, L.; Sun, Y.; Hu, E.; Ning, J.; Zhong, Y.; Zhang, Z.; Hu, Y. Facile In-Situ Growth of Ni_2P/Fe_2P Nanohybrids on Ni Foam for Highly Efficient Urea Electrolysis. *J. Colloid Interface Sci.* **2019**, *541*, 279−286.
(20) Li, J.; Wang, J.; Jiao, F.; Lin, Y.; Gong, Y. Heterostructured CoP/MoO_2 as High Efficient Electrocatalysts for Hydrogen Evolution Reaction over All pH Values. *Int. J. Hydrogen Energy* **2021**, *46*, 18353−18363.
(21) Ahmad, W.; Gao, Q.; Zhang, X. L.; Tan, W.; Zhang, L.; Gao, M. R.; Yu, S. H. Sandwich-Type Polyoxometalate Mediates Cobalt Diselenide for Hydrogen Evolution in Acidic Electrolyte. *ChemNanoMat* **2020**, *6*, 1164−1168.
(22) Zhang, J.; Zhang, Q.; Feng, X. Support and Interface Effects in Water-Splitting Electrocatalysts. *Adv. Mater.* **2019**, *31*, 1808167.
(23) Li, Z.; Hu, M.; Wang, P.; Liu, J.; Yao, J.; Li, C. Heterojunction Catalyst in Electrocatalytic Water Splitting. *Coord. Chem. Rev.* **2021**, *439*, 213953.
(24) Liu, D.; Ai, H.; Chen, M.; Zhou, P.; Li, B.; Liu, D.; Du, X.; Lo, K. H.; Ng, K. W.; Wang, S. P.; Chen, S.; Xing, G.; Hu, J.; Pan, H. Multi-Phase Heterostructure of CoNiP/Co_xP for Enhanced Hydrogen Evolution under Alkaline and Seawater Conditions by Promoting H_2O Dissociation. *Small* **2021**, *17*, 2007557.
(25) Sheng, S.; Ye, K.; Gao, Y.; Zhu, K.; Yan, J.; Wang, G.; Cao, D. Simultaneously Boosting Hydrogen Production and Ethanol Upgrading Using a Highly-Efficient Hollow Needle-Like Copper Cobalt Sulfide as a Bifunctional Electrocatalyst. *J. Colloid Interface Sci.* **2021**, *602*, 325−333.
(26) Yu, X.; Yu, Z.-Y.; Zhang, X.-L.; Li, P.; Sun, B.; Gao, X.; Yan, K.; Liu, H.; Duan, Y.; Gao, M.-R.; Wang, G.; Yu, S.-H. Highly Disordered Cobalt Oxide Nanostructure Induced by Sulfur Incorporation for Efficient Overall Water Splitting. *Nano Energy* **2020**, *71*, 104652.
(27) Wang, S.; Wang, Y.; Zang, S. Q.; Lou, X. W. Hierarchical Hollow Heterostructures for Photocatalytic CO_2 Reduction and Water Splitting. *Small Methods* **2020**, *4*, 1900586.
(28) Wu, D.; Chen, D.; Zhu, J.; Mu, S. Ultralow Ru Incorporated Amorphous Cobalt-Based Oxides for High-Current-Density Overall Water Splitting in Alkaline and Seawater Media. *Small* **2021**, *17*, 2102777.
(29) Anantharaj, S.; Noda, S. Amorphous Catalysts and Electrochemical Water Splitting: an Untold Story of Harmony. *Small* **2020**, *16*, 1905779.
(30) Yang, L.; Guo, Z.; Huang, J.; Xi, Y.; Gao, R.; Su, G.; Wang, W.; Cao, L.; Dong, B. Vertical Growth of 2D Amorphous $FePO_4$ Nanosheet on Ni Foam: Outer and Inner Structural Design for Superior Water Splitting. *Adv. Mater.* **2017**, *29*, 1704574.
(31) Xu, Q.; Yu, T.; Chen, J.; Qian, G.; Song, H.; Luo, L.; Chen, Y.; Liu, T.; Wang, Y.; Yin, S. Coupling Interface Constructions of $FeNi_3$-MoO_2 Heterostructures for Efficient Urea Oxidation and Hydrogen Evolution Reaction. *ACS Appl. Mater. Interfaces* **2021**, *13*, 16355−16363.
(32) Cheng, H.; Yang, N.; Liu, G.; Ge, Y.; Huang, J.; Yun, Q.; Du, Y.; Sun, C. J.; Chen, B.; Liu, J.; Zhang, H. Ligand-Exchange-Induced Amorphization of Pd Nanomaterials for Highly Efficient Electrocatalytic Hydrogen Evolution Reaction. *Adv. Mater.* **2020**, *32*, 1902964.
(33) Zhang, X.; Luo, Z.; Yu, P.; Cai, Y.; Du, Y.; Wu, D.; Gao, S.; Tan, C.; Li, Z.; Ren, M.; Osipowicz, T.; Chen, S.; Jiang, Z.; Li, J.; Huang, Y.; Yang, J.; Chen, Y.; Ang, C. Y.; Zhao, Y.; Wang, P.; Song, L.; Wu, X.; Liu, Z.; Borgna, A.; Zhang, H. Lithiation-Induced Amorphization of $Pd_3P_2S_8$ for Highly Efficient Hydrogen Evolution. *Nat. Catal.* **2018**, *1*, 460−468.
(34) Ge, J.; Yin, P.; Chen, Y.; Cheng, H.; Liu, J.; Chen, B.; Tan, C.; Yin, P. F.; Zheng, H. X.; Li, Q. Q.; Chen, S.; Xu, W.; Wang, X.; Wu, G.; Sun, R.; Shan, X. H.; Hong, X.; Zhang, H. Ultrathin Amorphous/Crystalline Heterophase Rh and Rh Alloy Nanosheets as Tandem Catalysts for Direct Indole Synthesis. *Adv. Mater.* **2021**, *33*, 2006711.
(35) Yang, N.; Cheng, H.; Liu, X.; Yun, Q.; Chen, Y.; Li, B.; Chen, B.; Zhang, Z.; Chen, X.; Lu, Q.; Huang, J.; Huang, Y.; Zong, Y.; Yang, Y.; Gu, L.; Zhang, H. Amorphous/Crystalline Hetero-Phase Pd Nanosheets: One-Pot Synthesis and Highly Selective Hydrogenation Reaction. *Adv. Mater.* **2018**, *30*, 1803234.
(36) Cheng, H.; Yang, N.; Liu, X.; Yun, Q.; Goh, M. H.; Chen, B.; Qi, X.; Lu, Q.; Chen, X.; Liu, W.; Gu, L.; Zhang, H. Aging Amorphous/Crystalline Heterophase PdCu Nanosheets for Catalytic Reactions. *Natl. Sci. Rev.* **2019**, *6*, 955−961.
(37) Jin, Y.; Wang, H.; Li, J.; Yue, X.; Han, Y.; Shen, P. K.; Cui, Y. Porous MoO_2 Nanosheets as Non-Noble Bifunctional Electrocatalysts for Overall Water Splitting. *Adv. Mater.* **2016**, *28*, 3785−3790.
(38) Zhou, E.; Wang, C.; Zhao, Q.; Li, Z.; Shao, M.; Deng, X.; Liu, X.; Xu, X. Facile Synthesis of MoO_2 Nanoparticles as High Performance Supercapacitor Electrodes and Photocatalysts. *Ceram. Int.* **2016**, *42*, 2198−2203.
(39) Haetge, J.; Djerdj, I.; Brezesinski, T. Nanocrystalline $NiMoO_4$ with an Ordered Mesoporous Morphology as Potential Material for Rechargeable Thin Film Lithium Batteries. *Chem. Commun.* **2012**, *48*, 6726−6728.
(40) Padmanathan, N.; Shao, H.; Razeeb, K. M. Honeycomb Micro/Nano-Architecture of Stable β-$NiMoO_4$ Electrode/Catalyst for Sustainable Energy Storage and Conversion Devices. *Int. J. Hydrogen Energy* **2020**, *45*, 30911−30923.
(41) Dong, Z.; Lin, F.; Yao, Y.; Jiao, L. Crystalline $Ni(OH)_2$/Amorphous $NiMoO_x$ Mixed-Catalyst with Pt-Like Performance for Hydrogen Production. *Adv. Energy Mater.* **2019**, *9*, 1902703.
(42) Podlaha, E. J.; Landolt, D. Induced Codeposition: III. Molybdenum Alloys with Nickel, Cobalt, and Iron. *J. Electrochem. Soc.* **1997**, *144*, 1672−1680.
(43) Wang, F.; Ma, K.; Tian, W.; Dong, J.; Han, H.; Wang, H.; Deng, K.; Yue, H.; Zhang, Y. X.; Jiang, W.; Ji, J. P-Doped $NiMoO_4$ Parallel Arrays Anchored on Cobalt Carbonate Hydroxide with Oxygen Vacancies and Mass Transfer Channels for Supercapacitors and Oxygen Evolution. *J. Mater. Chem. A* **2019**, *7*, 19589−19596.
(44) Du, W.; Shi, Y.; Zhou, W.; Yu, Y.; Zhang, B. Unveiling the in Situ Dissolution and Polymerization of Mo in Ni_4Mo Alloy for Promoting the Hydrogen Evolution Reaction. *Angew. Chem., Int. Ed.* **2021**, *60*, 7051−7055.
(45) Zhang, X.; Liu, P.; Sun, Y.; Zhan, T.; Liu, Q.; Tang, L.; Guo, J.; Xia, Y. $Ni_3[Fe(CN)_6]_2$ Nanocubes Boost the Catalytic Activity of Pt for Electrochemical Hydrogen Evolution. *Inorg. Chem. Front.* **2018**, *5*, 1683−1689.
(46) Yu, X.; Zhao, J.; Johnsson, M. Interfacial Engineering of Nickel Hydroxide on Cobalt Phosphide for Alkaline Water Electrocatalysis. *Adv. Funct. Mater.* **2021**, *31*, 2101578.
(47) Zhang, L.; Jang, H.; Liu, H.; Kim, M. G.; Yang, D.; Liu, S.; Liu, X.; Cho, J. Sodium-Decorated Amorphous/Crystalline RuO_2 with

https://doi.org/10.1021/acsomega.1c05844
ACS Omega 2022, 7, 2244−2251

Rich Oxygen Vacancies: a Robust pH-Universal Oxygen Evolution Electrocatalyst. *Angew. Chem., Int. Ed.* **2021**, *60*, 18821−18829.
(48) Dinh, C.-T.; Jain, A.; de Arquer, F. P. G.; De Luna, P.; Li, J.; Wang, N.; Zheng, X.; Cai, J.; Gregory, B. Z.; Voznyy, O.; Zhang, B.; Liu, M.; Sinton, D.; Crumlin, E. J.; Sargent, E. H. Multi-Site Electrocatalysts for Hydrogen Evolution in Neutral Media by Destabilization of Water Molecules. *Nat. Energy* **2019**, *4*, 107−114.
(49) Qiao, L.; Zhu, A.; Yang, H.; Zeng, W.; Dong, R.; Tan, P.; Zhong, D.; Ma, Q.; Pan, J. Copper-Nickel Embedded into a Nitrogen-Doped Carbon Octahedron as an Effective Bifunctional Electrocatalyst. *Inorg. Chem. Front.* **2018**, *5*, 2276−2283.
(50) Jiang, X.; Jang, H.; Liu, S.; Li, Z.; Kim, M. G.; Li, C.; Qin, Q.; Liu, X.; Cho, J. The Heterostructure of Ru_2P/WO_3/NPC Synergistically Promotes H_2O Dissociation for Improved Hydrogen Evolution. *Angew. Chem., Int. Ed.* **2021**, *60*, 4110−4116.
(51) Hu, J.; Fang, C.; Jiang, X.; Zhang, D.; Cui, Z. PtMn/PtCo Alloy Nanofascicles: Robust Electrocatalysts for Electrocatalytic Hydrogen Evolution Reaction under Both Acidic and Alkaline Conditions. *Inorg. Chem. Front.* **2020**, *7*, 4377−4386.
(52) Zhu, Y.; Tahini, H. A.; Hu, Z.; Chen, Z. G.; Zhou, W.; Komarek, A. C.; Lin, Q.; Lin, H. J.; Chen, C. T.; Zhong, Y.; Fernández-Díaz, M. T.; Smith, S. C.; Wang, H.; Liu, M.; Shao, Z. Boosting Oxygen Evolution Reaction by Creating Both Metal Ion and Lattice-Oxygen Active Sites in a Complex Oxide. *Adv. Mater.* **2020**, *32*, 1905025.
(53) Zhao, B.; Zhang, L.; Zhen, D.; Yoo, S.; Ding, Y.; Chen, D.; Chen, Y.; Zhang, Q.; Doyle, B.; Xiong, X.; Liu, M. A Tailored Double Perovskite Nanofiber Catalyst Enables Ultrafast Oxygen Evolution. *Nat. Commun.* **2017**, *8*, 14586.
(54) Hu, E.; Yao, Y.; Chen, Y.; Cui, Y.; Wang, Z.; Qian, G. Cu^{2+}-Guided Construction of the Amorphous $CoMoO_3$/Cu Nanocomposite for Highly Efficient Water Electrolysis. *ACS Appl. Energy Mater.* **2021**, *4*, 6740−6748.
(55) Zhong, B.; Zhang, L.; Yu, J.; Fan, K. Ultrafine iron-cobalt nanoparticles embedded in nitrogen-doped porous carbon matrix for oxygen reduction reaction and zinc-air batteries. *J. Colloid Interface Sci.* **2019**, *546*, 113−121.
(56) Mun, Y.; Lee, S.; Kim, K.; Kim, S.; Lee, S.; Han, J. W.; Lee, J. Versatile Strategy for Tuning ORR Activity of a Single Fe-N_4 Site by Controlling Electron-Withdrawing/Donating Properties of a Carbon Plane. *J. Am. Chem. Soc.* **2019**, *141*, 6254−6262.

https://doi.org/10.1021/acsomega.1c05844
ACS Omega 2022, 7, 2244−2251